Journal of Materials Chemistry C

ROYAL SOCIETY OF CHEMISTRY

PAPER

Published on 07 July 2026

Cite this: DOI: 10.1039/d6tc01214k

On phase separation and crystallization of Ge-rich GeSbTe alloys from atomistic simulations with a machine learning interatomic potential

Omar Abou El Kheir, Dario Baratella and Marco Bernasconi *

Received 16th April 2026,
Accepted 29th June 2026

DOI: 10.1039/d6tc01214k

rsc.li/materials-c

We developed a machine learning interatomic potential (MLIP) for Ge-rich GeSbTe alloys of interest for applications in phase change memories embedded in microcontrollers. The MLIP was generated by fitting with a neural network method a large database of energies and forces computed within density functional theory of elemental, binary, stoichiometric and non-stoichiometric ternary alloys in the Ge–Sb–Te phase diagram. The MLIP is demonstrated to be highly transferable to large regions of the phase diagram around the compositions included in the dataset. The MLIP is then exploited to simulate the crystallization with phase separation of three Ge-rich alloys on the $GeSb_2Te_3$ and $Ge–Ge_2Sb_2Te_5$ tie-lines that correspond to the set process of the memory cell. The transformation on the ns time scale and at 600 K, comparable to the operation conditions of the memory, yields crystalline cubic GeTe slightly Sb-doped and amorphous GeSb and Ge. These metastable phases differ from the thermodynamically stable products and form due to kinetics effects on the short time span of the set operation in phase change memories.

1. Introduction

Phase change memories (PCMs) are of interest for several applications, including stand-alone storage class memories,[1,2] in-memory and neuromorphic computing devices,[3,4] and embedded memories in microcontrollers.[5,6] These applications exploit a fast and reversible transformation between the crystalline and amorphous phases of a chalcogenide alloy, typically GeSbTe (GST),[7–9] induced by heating. Depending on the device architecture, heat is provided by current pulses either *via* Joule effects within the transforming material or *via* a resistive element, the heater, in contact with a thin film of GST. By applying an intense current pulse, crystalline GST is brought above the melting temperature and subsequently amorphizes due to fast cooling (reset process). By applying a less intense and longer current pulse, the amorphous phase recrystallizes (set process).

For embedded applications, the amorphous phase must sustain the thermal budget for the soldering process in which the device is exposed to 530 K for a few minutes. To meet this requirement, Ge-rich GST alloys (GGST) have been developed reaching a crystallization temperature T_x above 600 K for alloys on the $Ge–Sb_2Te_3$ tie-line,[10–13] which is much higher than that (T_x = 420–440 K[14]) of the flagship $Ge_2Sb_2Te_5$ (GST225) compound, mostly used for neuromorphic and stand-alone devices.[7–9] GGST has already been exploited in the next-generation microcontrollers (28 nm MOS technology).[15,16]

The increase in T_x comes at the cost of increased complexity in the set and reset processes. In fact, the crystallization of non-stoichiometric GGST alloys involves the segregation of Ge in excess and the formation of GST crystallites with a lower fraction of Ge.[11,12,17–24] The mass transport that accompanies this transformation slows the overall process, increasing T_x. The crystallization temperature can be further increased by doping with nitrogen[18,25–29] which was shown to reduce the mobility of Ge.[30]

For GGST alloys on the Ge-GST225 tie-line, which are often discussed in literature,[19–21,31] the transformation should yield pure Ge and GST225 from the thermodynamical point of view. In fact, in the ternary Ge–Sb–Te phase diagram, the only thermodynamically stable compounds lie on the $GeTe–Sb_2Te_3$ and $Sb–Sb_2Te_3$ tie-lines.[32] Indeed, heating GGST films for hours above T_x leads to the formation of face centered cubic (fcc) GST with a lattice parameter consistent with cubic GST on the $GeTe–Sb_2Te_3$ pseudobinary line.[17]

However, in the short time span of the set operation in the devices, kinetic effect might favor the formation of metastable phases or intermediate products preventing the transformation into the thermodynamically stable compounds. For example, experimental evidence was provided on the formation of GeTe as an intermediate product in the decomposition of GGST

Department of Materials Science, University of Milano-Bicocca, Via R. Cozzi 55, I-20125 Milano, Italy. E-mail: marco.bernasconi@unimib.it

films.[20,31] In ref. 31, Ge segregation and the formation of GeTe crystals were observed by annealing a GGST film above 310 °C. First, GeTe crystallizes in the metastable *Pnma* phase that triggers the crystallization of pure Ge and then evolves into the cubic phase. Only by further annealing at 410 °C, incorporation of Sb leads to the formation of crystallites with composition close to GST225.[31] In other works in which the temperature was probably sufficiently higher than T_x, the final products consisting of crystalline Ge and cubic GST were observed with GST crystallizing first.[21]

The likely possibility of formation of cubic GeTe in the decomposition process of GGST was actually predicted by our density functional theory (DFT) calculation of the convex hull in the Ge–Sb–Te phase diagram.[32] Knowledge of the DFT formation energy of all GST alloys in the central part of the Ge–Sb–Te ternary phase diagram allowed us to identify the metastable cubic crystalline phases, in addition to the themodynamically stable compounds in the GeTe–Sb_2Te_3 tie-line, which are more likely to form during the crystallization of a generic GST alloy.[32] It was shown that Sb-doped cubic GeTe was the most probable product in the decomposition of several Ge-rich alloys on the Ge–Sb_2Te_3, Ge-GST225 and Ge-GST124 tie-lines.[23,24,32,33]

In the real device, the transformation is further affected by the presence of temperature gradients and high electric fields that drive atoms with effective charges of different sign in opposite directions. An example of the complex nanostructure arising in the GGST-PCM is provided in ref. 34 where scanning transmission electron microscopy (TEM), energy dispersive X-ray (EDX) and electron energy loss spectroscopy (EELS) were used to characterize a PCM cell after the forming operation, *i.e.* the first cycle of melting and recrystallization of an active dome embedded in a polycrystalline matrix, resulting in turn from uniform heating of the as-deposited amorphous homogeneous alloy. This analysis revealed a complex nanostructure formed by a core more Sb-rich and a Ge-rich shell with evidence of formation of GeTe crystallites above the dome and trigonal Sb crystallites inside the dome.[34] However, EELS and EDX measurements are averaged over different grains along the direction of the beam which introduces uncertainties in the composition of the crystallites.

Another issue for the operation of GGST-PCMS, is the presence of a drift in the electrical resistance with time in both the set and reset states. The resistance drift in the reset state (amorphous phase) is ascribed to structural relaxations towards a more stable amorphous structure and is common to all phase change materials. On the contrary, the resistance drift in the set state (crystalline), is peculiar to GGST alloys. This feature was ascribed to the particular microstructure resulting from crystallization with phase separation that generates a residual amorphous Ge region close to the heater.[35] However, many details about the role of the electric field, and thermal gradient in assigning the morphology of the polycrystalline matrix that embeds the transforming material are still unclear.

In this respect, atomistic simulations can provide useful information on the parameters that control possible different decomposition pathways in this complex system. We have already mentioned that DFT calculations provided information on the decomposition propensity of GGST alloys and the most likely decomposition path during crystallization based on thermochemical data.[32] The stability of homogeneous GGST alloys with respect to phase separation in still amorphous products was also addressed by DFT molecular dynamics (MD) in ref. 36 where it was shown that segregation of Ge in the amorphous phase is expected for a Ge content greater than 50%. However, these latter works only considered the thermodynamical aspects of the phase transformation and not possible kinetics effects due to the limitations in the size and time scale of DFT-MD simulations. These limitations can be overcome by MD simulations with machine learning interatomic potentials (MLIP) generated by training over a large database (DB) of DFT energies.[37–40] MLIP simulations of the crystallization process have been reported in literature for some stoichiometric phase change alloys including GeTe[41,42] and GST225.[43–45] MLIP-MD simulations of the Sb-rich $Ge_3Sb_6Te_5$ alloy were also recently reported,[46] showing crystallization in a metastable off-stoichiometric cubic phase without phase separation.

In a previous work, we have shown that crystallization and decomposition of simpler binary Ge-rich Ge_xTe alloys can be simulated on the ns time scale by MLIP-MD.[47] To summarize in brief the results of ref. 47, simulations with 32 000-atom models showed that the crystallization mechanism of Ge_2Te depends on temperature. At 600 K, segregation of most Ge in excess occurred on the ns time scale followed by the crystallization of a nearly stoichiometric GeTe region. Instead, at 500 K, nuclei of crystalline GeTe form before phase separation and then grow slowly due to the concurrent expulsion of Ge in excess. On the other hand, we have also utilized a MLIP for stoichiometric GST225 to simulate the set process in a multimillion atom model of a PCM[44] in the Wall architecture typically used for embedded memories.[16] These device-scale simulations, in which an amorphous dome was embedded in a crystalline matrix, provided a vivid picture of the subtle interplay between crystal nucleation and crystal growth from the amorphous-crystalline rim showing that in this geometry recrystallization is dominated by crystal growth at the crystal-amorphous interface.

In the perspective of simulating the set process of embedded memories at the device scale, here we develop a MLIP for GGST alloys by leveraging our previous works on Ge-rich Ge_xTe[47] and stoichiometric GST225[43] and using the DeePMD code.[48,49] The neural network (NN) scheme implemented in DeePMD was trained on a DFT-DB including the elemental, stoichiometric binary and ternary compounds, and the Ge-rich $Ge_5Sb_2Te_3$ (GST523) alloy on the Ge–Sb_2Te_3 tie-line. The training database also includes the DBs of the stoichiometric GST225[43] and the Ge-rich Ge_2Te alloys,[47] generated previously. The GST523 alloy was studied in previous experimental[11,24] and theoretical[33] works, and was also shown to be the constituent of the active region of PCMs cells in the reset state after forming from alloys richer in Ge (see Fig. 7 in ref. 50).

Since we aim at simulating the decomposition process of the alloy, the MLIP must be able to reproduce not only the starting

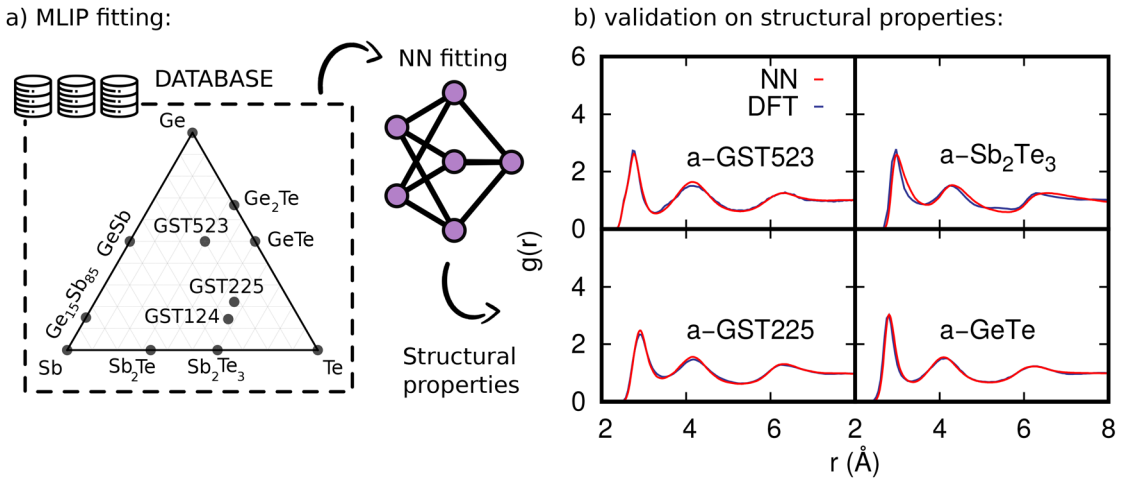

Fig. 1 (a) The ternary Ge–Sb–Te phase diagram showing the systems (dots) included in the training database of the MLIP. (b) Total pair correlation functions of amorphous GST523, GST225, Sb_2Te_3 and GeTe from MLIP (NN, red curves) and DFT (blue curves) simulations at 300 K. Details on these simulations are given in Section S2 of the SI.

and the final compositions, but also the intermediate phases/compositions that the system could visit during the transformation process. The MLIP must then be transferable to compositions not present in the training DB. We will show that the MLIP is indeed capable of describing alloys within a large region around GST523 in the ternary phase diagram. This includes the triangular region with the GST523, GeTe and Ge_2Te alloys, all present in the training DB, at the vertices (see Fig. 1a).

The MLIP was then utilized to simulate the crystallization with phase separation of GST523 on the Ge–Sb_2Te_3 tie-line, of the $Ge_7Sb_2Te_5$ (GST725) alloy with the same fraction of Ge (50%), but lying on the Ge-GST225 tie-line, and finally of the $Ge_{9.6}Sb_2Te_5$ alloy which lies very close to the intersection between the GST523-Ge_2Te and the Ge-GST225 lines (see Fig. 1a). Although thermodynamics predicts that the products of the crystallization would consist of the extremes of the tie-lines of the ternary phase diagram, the simulations show that kinetics effects lead to the formation of intermediate products that are the only phases visible on the ns time scale of the set process in the device. Namely, these unprecedented simulations reveal that, on the ns time scale, GGST alloys transform into crystalline, slightly Sb-doped, GeTe and Ge and Ge/Sb amorphous regions, which confirms the evidence of the presence of GeTe crystallites inferred from recent EDX/EELS measurements on the device.[34]

2. Methods

We generated the MLIP for GGST alloys by fitting a DB of DFT energies, forces, and virial tensors within the NN framework implemented in the DeePMD code.[48,49,51] To this end, we exploited the DB generated previously for GST225 compound and Ge-rich Ge_xTe alloys, and extended it to a wider range of compositions in the Ge–Sb–Te ternary phase diagram. The final DB consists of about 470 000 configurations of small cells in the amorphous and liquid phases and in the crystalline phases for the elemental and stoichiometric compounds that include (1) elemental Ge, Sb and Te, (2) the stoichiometric GeTe, Sb_2Te and Sb_2Te_3 binary compounds, (3) the off-stoichiometric Ge_2Te, $Ge_{15}Sb_{85}$ and GeSb binary alloys, (4) the stoichiometric GST225 and $GeSb_2Te_4$ ternary compounds, (5) the off-stoichiometric Ge-rich GST523 alloy, (6) crystalline superlattices GeTe-GST225, Sb_2Te_3-GST225, GST326-GST124. The compositions included in the DB are highlighted in the ternary Ge–Sb–Te phase diagram in Fig. 1a. The number of configurations and the cell sizes of each system are reported in Table S1 in the SI.

The atomic configurations were extracted from DFT molecular dynamics (MD) simulations by using the CP2k code.[52] The Perdew-Burke-Ernzherof (PBE) exchange and correlation functional[53] and Goedecker–Teter–Hutter (GTH) norm conserving pseudopotentials with s and p valence electrons were used.[54,55] Kohn–Sham orbitals were expanded in a triple-zeta-valence-plus-polarization (TZVP) basis set while the electronic density was expanded in plane waves up to a kinetic cutoff of 100 Ry. The Brillouin zone (BZ) integration was restricted to the Γ-point in all MD simulations. The time step was set to 2 fs and configurations were extracted every 100–200 fs. We recalculated energies, forces, and stresses for each configuration added to the DB with a higher accuracy by increasing the kinetic energy cutoff for the plane-waves expansion of the electronic density to 400 Ry and by using a $3 \times 3 \times 3$ or $4 \times 4 \times 4$ k-point mesh for the BZ integration. A Fermi–Dirac smearing in the occupation of Kohn–Sham states was used with an electronic temperature of 300 K.

In NN schemes for the generation of interatomic potentials, the total energy of the system is written as the sum of individual atomic energies that depend on the local environment of each atom.[37] In the DeePMD scheme the local environment is encoded by local descriptors which are generated by an embedded neural network. A second neural network (fitting

network) is built for the calculation of energies and forces with the local descriptors as input layer. We designed the embedded network with three hidden layers of 20, 40, and 80 nodes supplemented by other two layers with attention-based mechanism whose length is 128. The cutoff radius r_c was set to 7 Å, which is beyond the third coordination shell of our systems, while the smoothing radius r_s was set to 0.5 Å in the implementation of ref. 49. The maximum number of neighbors was set to 79. Finally, the network for the fitting of energy and forces consists of 4 hidden layers with 240 nodes each. In the embedding and fitting network, we have used the hyperbolic tangent as an activation function.

The MLIP was generated in an iterative manner. A first MLIP was generated by training over the DB of GST225 and Ge_xTe, supplemented with about 5000 configurations of GST523. Then, the MLIP is used to perform MD simulations that provide configurations from unexplored region of the configurational space to enrich the training DB for a second generation of the potential. In this step we performed metadynamics simulations[56–58] designed to accelerate the segregation of Ge in GGST alloys, and to collect configurations that include Ge–GeSbTe interfaces. We performed different simulations by using as collective variable one of the partial coordination numbers Ge–Ge, Ge–Sb or Ge–Te to promote the formation of Ge-rich regions in contact with Ge-poor regions. This step was crucial to accurately describe the interface energies and, hence, the barriers for the phase separation of GGST alloys. At the same time we enriched the DB with additional atomic configurations extracted from DFT-MD simulations with different compositions, at different densities and exploring a wider temperature range. We iterated the procedure until the error on forces and energies did not improve any more nor the validation on the structural properties of the liquid, amorphous and crystalline phases improved further with respect to the very good results that we will illustrate in Section 3.1. Structural and dynamical properties obtained from MLIP simulations were compared with results from DFT-MD simulations performed with the CP2k code with the same parameters given above. MLIP-MD simulations were performed by using the LAMMPS code[59] as MD driver with the DeePMD plugin.

To assess whether an atom is crystalline in the simulations of the crystallization process, we used the Steinhardt order parameters Q_4^{dot} (ref. 60 and 61) defined for each atom i by

$$Q_4^{\mathrm{dot}} = \frac{1}{N_i}\sqrt{\sum_{j=1}^{N_i}\sum_{m=-4}^{4} q_{4m,i}q_{4m,j}^{*}}; \quad q_{4m,i} = \frac{1}{N_i}\sum_{j=1}^{N_i} Y_{4m}(\hat{\mathbf{r}}_{ij}) \quad (1)$$

where N_i in the number of neighbors of atom i up to a given cutoff, j is the neighbors index, Y_{4m} is the 4th spherical harmonic with degree m, and $\hat{\mathbf{r}}_{ij}$ is the unit vector connecting the two atoms. A threshold of $Q_4^{\mathrm{dot}} = 0.80$ was chosen for an atom to be crystalline.

To identify the products of the decomposition process of GGST we used the Smooth Overlap of Atomic Position similarity kernel (SOAP).[62] In the SOAP formalism, the local atomic density around each atom j is expressed as a sum of Gaussian functions (here with broadening σ_{at} = 0.5 Å) centered on the position of its neighbors up to a given cutoff (here 9–12 Å). Then, the density around atom j is expanded in spherical harmonics and radial basis functions $g_{\mathbf{b}}$ ($|\mathbf{r}|$) as $\rho_j(\boldsymbol{r}) = \sum_{blm} c_{blm} g_b(|\mathbf{r}|) Y_{lm}(\hat{\mathbf{r}})$. The coefficients of this expansion define the so-called power spectrum matrix $p(j)_{b_1 b_2 l} = \pi\sqrt{8/(2l+1)} \sum_m \left(c_{b_1 lm}\right)^* c_{b_2 lm}$ whose elements are turned into a vector $\mathbf{p}_j$ which is calculated for each atom for several configurations along the MD trajectories. Then, we performed a principal component analysis (PCA)[63] over the set of vectors $\mathbf{p}_j$, which were then clustered in the PCA space with the k-means algorithm.[64] Finally, we labeled each atom according to the cluster index, which allowed us to define distinct chemical and structural environments and their evolution in time directly from the MD trajectories. The SOAP kernel was computed using the DScribe Python package[65,66] and the ASE Python library[67] while for the PCA and the clustering analysis with k-means algorithm, we used the scikit-learn python package.[68]

3. Results and discussion

3.1. Validation of the potential

The accuracy of the MLIP is assessed by the root mean square error (RMSE) on energies and forces reported for each system in our DB (see Table S1 in SI). The position in the ternary Ge–Sb–Te phase diagram of the systems included in the training DB is shown in Fig. 1a. The average RMSE of the MLIP over the whole training data set is 7.62 meV per atom on energy and 148 meV $Å^{-1}$ on forces which is very close to the RMSE on the test data set of 7.7 meV per atom and 148 meV $Å^{-1}$. Typical average error obtained with DeePMD for highly disordered multicomponent systems are in the range 2–7 meV per atom and 90–145 meV $Å^{-1}$ (ref. 69–72).

The accuracy of the MLIP is further assessed by comparing the structural properties of the liquid, amorphous and crystalline phases of the different systems included in the database with reference DFT calculations. As an example, we show the total pair correlation function of amorphous GST225, GST523, Sb_2Te_3 and GeTe in Fig. 1b. A comprehensive analysis of the structural properties of all systems in the training DB is provided in Section S2 of the SI, which includes the partial pair correlation functions, the distribution of coordination numbers, the average partial coordination numbers, the angle distribution functions for each chemical species in amorphous and liquid phases. Moreover, it is well known that Ge in amorphous GST alloys can features different local environments: a tetrahedral geometry (4-fold coordinated), a pyramidal geometry (3-fold coordinated) and defective octahedral geometry (octahedral angles but coordination lower than six). The fraction of Ge atoms in tetrahedral configurations can be quantified by using the q-parameter for tetrahedricity introduced in ref. 73 and used for GST225 in ref. 74. The q-parameter is reported for the all amorphous alloys in the SI. We assessed the accuracy of the MLIP for the crystalline phases

by computing the equation of state (energy as a function of volume) and its fit with the Birch–Murnaghan function which yields the equilibrium energy and density and the bulk modulus (see Section 2 in SI).

Overall, the MLIP describes well all phases of all compositions. The largest error is on the equilibrium density of crystalline Te and Sb_2Te_3 which is overestimated by about 2 and 1.5% compared to reference data.

Since we are interested in reproducing the crystallization kinetics of GGST alloys which involves Ge segregation, the MLIP must be able to describe not only the starting and final compositions, but also all the intermediate compositions visited during the transformation process. Therefore, the MLIP must be transferable to a wide range of compositions around those present in the training DB. The MLIP was then cross-validated by evaluating the RMSE on compositions not seen during training. In this test set, we included compositions on the GeSb–GeTe line, Sb–GeTe line and configurations of the a-Ge/a-GeTe interface (see Fig. 2a and b). The average RMSE on energies and forces, reported in Table S2 in the SI, is very similar to the average RMSE on the training database.

Moreover, we assessed the transferability of the MLIP by evaluating the structural properties of the amorphous phase of four GGST alloys. Two alloys along the Ge-GST225 tie-line, namely $Ge_7Sb_2Te_5$ (GST725, or Ge_{36}-GST in the notation of ref. 21 which stands for 36% of Ge and 64% of GST225, which means a total of 36 + 64 × 2/9% of Ge) and $Ge_{9.6}Sb_2Te_5$ ($Ge_{58}Sb_{12}Te_{30}$, or Ge_{46}-GST in the notation of ref. 21). The $Ge_{9.6}Sb_2Te_5$ alloy is close to the intersection between the Ge-GST225 tie-line and the GST523-Ge_2Te line. The other two alloys $Ge_4Sb_2Te_3$ (GST423) and $Ge_3Sb_2Te_3$ (GST323) lye along the Ge–Sb_2Te_3 tie-line. As an example here, in Fig. 2c we compare the total pair correlation functions from NN and DFT simulations for GST725 and $Ge_{9.6}Sb_2Te_5$. Other structural properties are discussed in Section S3 of the SI. Regarding the Ge–Sb_2Te_3 tie-line, we report the fraction of Ge–Ge homopolar bonds and the fraction of Ge in tetrahedral geometry in the amorphous phase as a function of Ge fraction in the alloy (see Fig. 2d where NN data are compared with DFT data from ref. 33). For the generation of these latter amorphous models we included the semiempirical van der Waals (vdW) corrections D3[75] for consistency with the DFT calculations in ref. 33 we compare with. Other structural properties of these amorphous alloys are discussed Section S3 of the SI.

Overall, the MLIP reproduces well the reference data of energies and forces in both the training and transferability

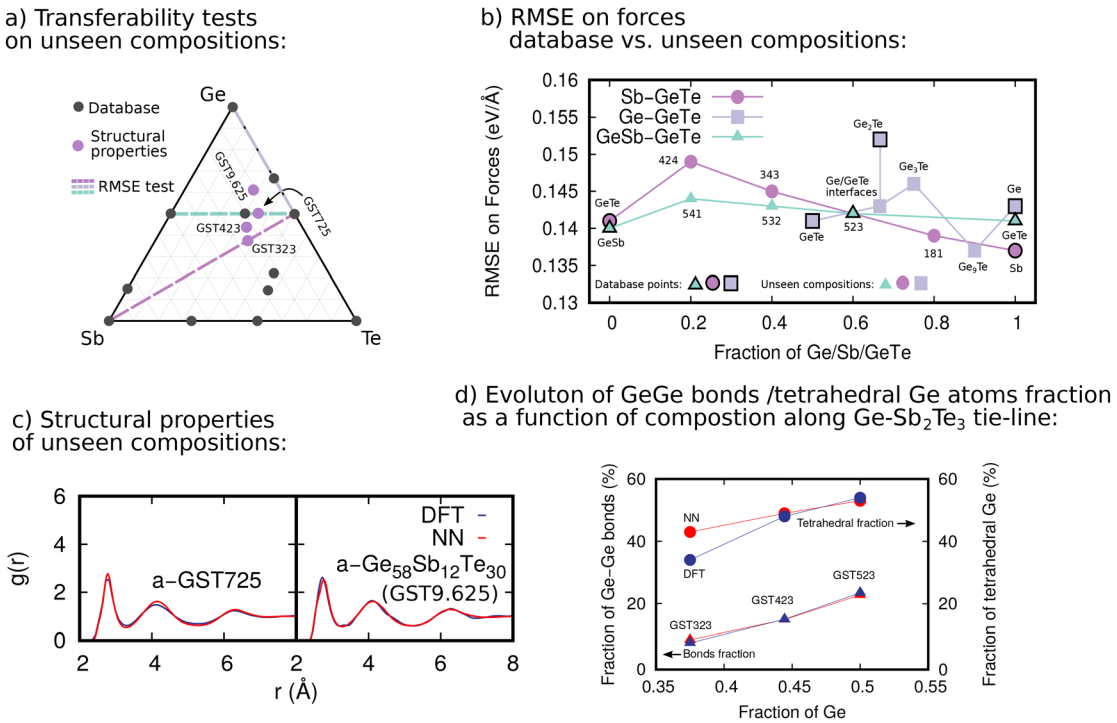

Fig. 2 (a) The Ge–Sb–Te ternary phase diagram with the systems included in the transferability test of the MLIP. The systems in the training DB are depicted with black dots. A few compositions not present in the training DB along the dashed lines were used as a test set of the MLIP by computing the RMSE on energies and forces. For this analysis, we considered alloys along the Sb–GeTe line (Sb-rich), Ge–GeTe (Ge-rich) and GeSb–GeTe line (both Sb-rich and Ge-rich). Finally, the violet points indicate alloys not seen in the training on which the MLIP was validated by computing the structural properties of the amorphous phase ($Ge_{9.6}Sb_2Te_5$, GST725, GST423, GST323). (b) The RMSE on forces for unseen compositions along the three lines in panel (a), and for alloys in the DB (symbols with black border). (c) Total pair correlation function of amorphous GST723 and $Ge_{9.6}Sb_2Te_5$ from MLIP (NN, red curves) and DFT (blue curves) simulations. Simulation details are given in Section S3 of the SI. (d) Fraction (%) of Ge atoms in tetrahedral geometry (dots) and of Ge–Ge homopolar bonds over the total number of bonds (triangles) as a function of Ge content (%) in different alloys along the Ge–Sb_2Te_3 tie-line from MLIP (NN, red) and DFT (blue) simulations. DFT data are taken from ref. 33. Simulation details are given in Section S3 of the SI.

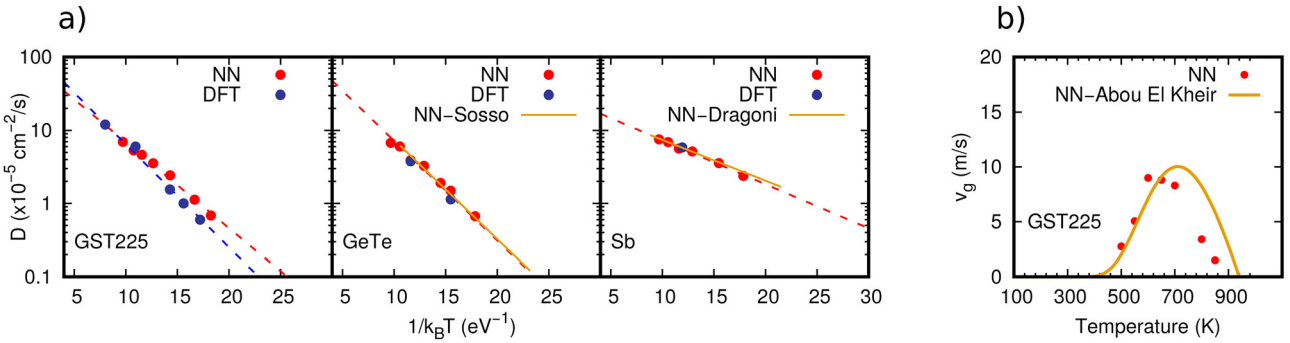

Fig. 3 (a) The Arrhenius plot (red dashed lines and red dots) of the self-diffusion coefficient D for GST225, GeTe and Sb. Data on GST225 are compared with previous DFT results from ref. 76 (blue dots and dashed line). Data on GeTe are compared with DFT results at two temperatures (blue dots) while the Arrhenius fit (red dashed line) is compared to previous results from NN simulations (orange continuous line) by Sosso *et al.*[79] Data on Sb are compared at one temperature with DFT results (blue dot) from ref. 80 while the Arrhenius fit (red dashed line) is compared to previous results from NN simulations (orange continuous line) by Dragoni *et al.*[78] (b) Crystal growth velocities (v_g) from present NN-MD simulations of GST225 compared with previous NN-MD simulations with a MLIP trained on GST225 in ref. 43 (continuous orange lines referring to the fitting of v_g with the Wilson-Frenkel phenomenological formula (see ref. 43)).

set. The MLIP describes very well the structural properties of all systems in the DB and of several alloys outside the training DB. In particular, the MLIP is able to reproduce the structural properties of alloys along the three lines GST523-Sb_2Te_3, GST523-GeTe and GST523-Ge_2Te whose end points are all included in the training DB.

Finally, we assessed the ability of the MLIP in reproducing the dynamical properties in the liquid and supercooled liquid phases. The self-diffusion coefficient D as a function of temperature is shown in Fig. 3a for GST225, GeTe and Sb as obtained from the present MLIP-MD simulations and from previous DFT-MD or MLIP-MD simulations. D is computed from the mean square displacement (MSD) and the Einstein relation MSD = $6Dt$ at long time t. In the temperature range of Fig. 3a, D can be described by an Arrhenius function $D = D_0 \exp(-E_a/k_BT)$. The activation energy E_a for GST225, GeTe and Sb from MLIP-MD (reference data) simulations is 0.270 ± 0.01 (0.333),[76] 0.310 ± 0.01 (0.296)[77] and 0.140 ± 0.005 (0.130)[78] eV. In supercooled liquid GST523 at 835 K the MLIP-MD self-diffusion coefficient of 4.1 ± 0.4 × 10^{-5} cm^2 s^{-1} is very close to the result of 3.8 × 10^{-5} cm^2 s^{-1} from previous DFT-MD simulations[33] In these last simulations on GST523, we used the D3 vdW corrections[75] for consistency with the previous DFT work we compare with.[33] Therefore, the MLIP reproduces well also previous results in the literature on the self-diffusion coefficient from DFT-PBE or MLIP-MD simulations fitted on DFT-PBE data.

We took a step further by simulating the heterogeneous crystallization process in GST225. The crystal growth velocities from the present MLIP-MD simulations are compared with MLIP-MD results from previous works in Fig. 3b. We remark that with our MLIP the melting temperature T_m for GST225 is 870 ± 5 K, which is slightly closer to the experimental value of 900 K[81] than the value of 940 K obtained with the previous MLIP for GST225 of ref. 43. To estimate T_m we used the same phase coexistence protocol described in our previous work.[43]

We remark that so far we have validated the MLIP by comparison to DFT-PBE data and to results from previous MLIP-MD simulations with potentials fitted on DFT-PBE data. The reliability of the DFT-PBE framework in describing the experimental structural and dynamical properties of phase change alloys and, in particular, GST225 has been discussed in several previous works,[9,74,82–84] to which we refer for a comprehensive analysis. We just mention that by adding vdW D2[85] corrections to our previous MLIP potential for GST225[43] a very good agreement with the experiments is achieved with regard to the crystal growth velocities[84] and the viscosity of the liquid.[86]

In conclusion, we judge that our MLIP is sufficiently accurate to investigate the kinetics of crystallization and phase separation in GGST that is discussed in the next section.

4. Simulation of the decomposition and crystallization process of Ge-rich GST alloys

The MLIP was exploited to simulate the crystallization and phase separation process of GGST alloys. We considered the three compositions already discussed in Section 3.1, namely GST523 on the Ge-Sb_2Te_3 tie-line and GST725 on the Ge-GST225 tie-line which have the same Ge fraction (50%). The third system is the $Ge_{9.6}Sb_2Te_5$ alloy ($Ge_{58}Sb_{12}Te_{30}$, Ge_{46}-GST in the notation of ref. 21) that is richer in Ge (58%) and lies on the Ge-GST225 tie-line. All simulations were performed at 600 K and at constant volume, consistent with the actual operation conditions of the memory.

As we mentioned in Section 1, from a thermodynamical point of view, GGST alloys are supposed to decompose into Ge and stoichiometric GST compounds on the Sb_2Te_3–GeTe tie-line. However, only the first stages of the transformation might be completed on the short time span of the programming operations of the memory, and kinetic effects could give rise to metastable intermediate phases as discussed in the introduction.

On these premises, we investigated the crystallization with phase separation aiming at identifying the intermediate products that form on the ns time scale at 600 K.

In the case of GST523, we used a 14 080-atom supercell at the theoretical equilibrium density of amorphous GST523 (0.0338 atom per Å^3)[87] obtained in our previous work.[33] Assuming that at the very end, GST523 decomposes into the thermodynamically favored products (Ge and Sb_2Te_3), and that Ge segregates into the amorphous phase at its equilibrium density (0.0438 atom per Å^3),[88] the density of the remaining Sb_2Te_3-like region would be 0.0275 atom per Å^3, which is very close to the experimental density of the liquid at 1003 K (0.0281 atom per Å^3).[89] We started from a model equilibrated at 1400 K for 20 ps, followed by a second equilibration at 1000 K for 20 ps, and then by a rapid quenching to 600 K in 40 ps. Once we reached the target temperature, we simulated the crystallization with phase separation for about 6 ns at NVT conditions. The SOAP analysis described in Section 2 was then performed over the whole trajectory. The cluster analysis (see Section 2) yielded ten different environments that have been identified by cross-checking with the distribution of the different chemical species. The ten environments are described in Table 1.

The time evolution of the fraction of atoms belonging to the different ten SOAP environments is shown in Fig. 4a together with the fraction of crystalline atoms identified by the Q_4^{dot} order parameter for crystallinity (see Section 2). Snapshots at an early stage (0.08 ns), an intermediate stage (0.8 ns) and at the end of the simulation are shown in Fig. 4b–d which reports the atoms colored according to the chemical species (on the left) and according to the SOAP environment (on the right). At the beginning of the simulation (Fig. 4b), the system is almost homogeneous and consists of Sb, Ge and Te in homogeneous GST523 (SOAP environments 5,6,8, see Table 1). In the intermediate and final snapshots (Fig. 4c and d), Te and Ge atoms in GeTe-like region are found (SOAP environments 2 and 3). The decomposition also leads to the appearance of Sb and Ge atoms in GeSb-like regions (SOAP environments 4 and 9) and atoms at the interface between GeTe-like and GeSb-like regions (SOAP environments 1, 7 and 10).

In the simulation, phase separation starts almost immediately, as was the case for Ge_2Te.[47] In the time evolution in Fig. 4, we first observed an increase in the fraction of interfacial Ge and Sb atoms (SOAP environments 1 and 7), followed by the formation of a GeTe-like region (SOAP environments 2 and 3). Subsequently, GeSb-like regions appear (SOAP environments 4 and 9). After about 2 ns the transformation products reach a plateau. Once phase separation was completed, we observed a coarsening of the different GeSb regions formed during the previous steps, as shown in Fig. 4c and d (SOAP environments 4 and 9). Finally, a GeTe-like crystalline nucleus forms and grows after about 5 ns (black curve in Fig. 4a) until it reaches a saturation corresponding to complete crystallization of the GeTe-like regions that percolate through the cell along the three cartesian directions (see Fig. 4d). The products of the crystallization and phase separation of GST523 on the ns time scale are thus crystalline $Ge_{12}SbTe_{12}$ (slightly Sb-doped GeTe) in

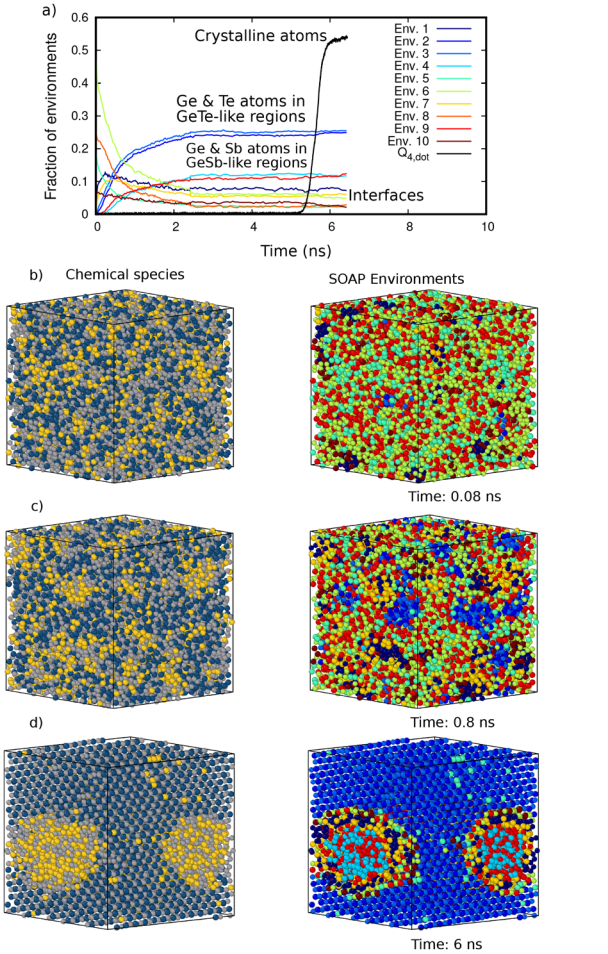

Fig. 4 (a) Evolution in time of the fraction of atoms in the ten different SOAP environments and of the Q_4^{dot} order parameter for crystallinity, during the crystallization of GST523 at 600 K. The description of the different environments is given in Table 1. Snapshot of the transformation process (b) at the beginning, (c) at an intermediate time and (d) at the end of the simulation. In the panels on the left atoms are colored according to the chemical species (Ge, Sb, Te in gray, yellow and blue). In the panels on the right, atoms are colored according to the different SOAP environments whose color code is given in panel (a). The Ovito[90] tool was used for the visualization and the generation of all atomic snapshots of this article.

Table 1 Description of the ten different environments identified by the SOAP and cluster analysis (see Section 2) during the transformation of the three alloys GST523, GST725 and $Ge_{9.6}Sb_2Te_5$ at 600 K

Environment number	Description
1	Ge atoms at interfaces
2	Te atoms in GeTe-like regions
3	Ge atoms in GeTe-like regions
4	Sb in GeSb-like regions for GST523 and GST725; Ge and Sb in GeSb-like regions for $Ge_{9.6}Sb_2Te_5$
5	Sb in homogeneous GST
6	Ge in homogeneous GST
7	Sb atoms at interfaces
8	Te in homogeneous GST
9	Ge in GeSb-like region for GST523 and GST725; pure Ge atoms for $Ge_{9.6}Sb_2Te_5$
10	Te atoms at interfaces (present only in GST523)

the cubic (β) phase and amorphous $Ge_{52}Sb_{48}$, instead of the thermodynamically favored Ge and Sb_2Te_3 crystals. We remark that at the end of the simulation the cluster analysis assigns to environments 5,6,8 (homogeneous untransformed GST) atoms that are actually at the interfaces between crystalline GeTe and amorphous GeSb/Ge but that clearly belong to one of these two regions. Therefore, the fraction of residual untransformed GST is smaller than the value given in Fig. 4a. Nucleation is a stochastic process, and thus the observation of a single nucleation event just sets the time scale for the nucleation time, but it is not a quantitative estimate, as in a Poissonian process the variance is equal to the mean. Moreover, we expect to have underestimated the nucleation time due to the lack of vdW corrections to the MLIP trained on the PBE database. In fact, from previous work on stoichiometric GeTe[91] and GST225[84] we know that the addition of vdW D2[85] corrections leads to an increase in the nucleation time and a decrease of the crystal growth velocity. Therefore, we repeated the simulation of GST523 crystallization by adding vdW corrections (D3).[75] Phase separation occurs in about 3 ns similarly to simulations without vdW corrections, but nucleation of crystalline GeTe took 9.5 ns instead of 5 ns (see above). Therefore, a more reliable estimate of the nucleation time of crystalline GeTe to be compared with experiments on GGST is a few tens of ns. We note that 600 K is close to the $\alpha \rightarrow \beta$ transition of GeTe experimentally detected at 705 K[92] or 600 K in a more recent work,[93] which prevented us from seeing the trigonal distortion of the α-phase.[94] The small Sb content can also stabilize the cubic phase of GeTe against the trigonal phase.

Very similar results were observed for the crystallization of GST725 on the Ge-GST225 tie-line (see Section S4 in SI for more details). In this case, the products of crystallization and phase separation is cubic $Ge_{12}SbTe_{12}$ and amorphous $Ge_{54}Sb_{46}$ instead of Ge and GST225 as expected from thermodynamics. These simulations suggest that the transformation of GST523 and GST725 on the ns time scale is controlled by kinetics.

Switching to crystallization with phase separation of $Ge_{9.\bar{6}}Sb_2Te_5$, we used an 8000-atom simulation box at the theoretical density of the liquid phase at 1000 K estimated form NPT simulation (0.03359 atom per Å^3, See Section S3 of SI). Similarly to GST523, by assuming that $Ge_{9.\bar{6}}Sb_2Te_5$ will decompose into the thermodynamically favored products (Ge and GST225), and that Ge will segregate into the amorphous phase at its equilibrium density, the density of the remaining GST225 is 0.03111 atom per Å^3 which is very close to the experimental density of the amorphous phase (0.0309 atom per Å^3). We followed the same protocol used for GST523, by quenching from 1400 K to 600 K, followed by about 3.2 ns simulation of the crystallization with phase separation. Then, we performed the SOAP analysis as described above for GST523. The cluster analysis (see Section 2) yielded the same environments identified in GST523 (see Table 1), but for interfacial Te atoms that were not found in this latter alloy richer in Ge.

The time evolution of the fraction of atoms belonging to the different nine SOAP environments is shown in Fig. 5a together with the fraction of crystalline atoms identified by the Q_4^{dot} order parameter for crystallinity (see Section 2). Snapshots at an early stage (0.08 ns) and at the end of the simulation are shown in Fig. 5b and c which reports atoms colored according to the chemical species (on the left) and according to the SOAP environment (on the right). The results are very similar to those of GST523 and GST725. First, a separation into amorphous (supercooled liquid) GeTe-like and Ge–Sb-like regions is observed and then, after the phase separation was completed, crystal nucleation and growth was observed within the GeTe-like regions. A cubic GeTe crystal slightly Sb-doped percolates through the simulation cell along the three directions (see Fig. 5b and c). As opposed to GST523 and GST725, for the more Ge-rich $Ge_{9.\bar{6}}Sb_2Te_5$ alloy, we also observed regions of pure amorphous Ge.

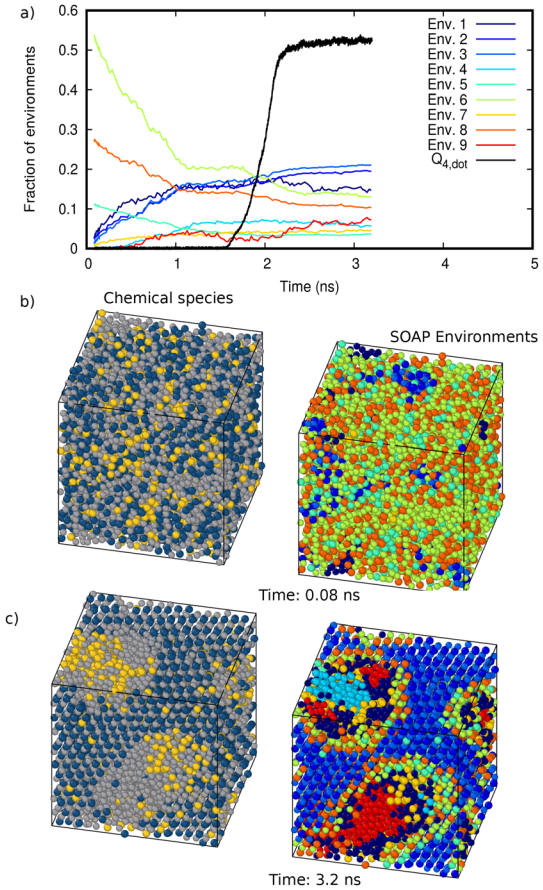

Fig. 5 (a) Evolution in time of the fraction of atoms in the nine different SOAP environments and of the Q_4^{dot} order parameter for crystallinity, during the crystallization of $Ge_{9.\bar{6}}Sb_2Te_5$ at 600 K. The description of the different environments is given in Table 1. Snapshot of the transformation process (b) at the beginning and (c) at the end of the simulation. In the panels on the left atoms are colored according to the chemical species (Ge, Sb, Te in gray, yellow and blue). In the panels on the right, atoms are colored according to the different SOAP environments whose color code is given in panel (a).

The products of the crystallization and phase separation of $Ge_{9.\bar{6}}Sb_2Te_5$ on the ns time scale are finally crystalline cubic $Ge_{48}Sb_5Te_{47}$, two pure Ge clusters and two amorphous $Ge_{46}Sb_{54}$ clusters, instead of the thermodynamically favored Ge and GST225 crystals.

We also repeated the simulation of $Ge_{9.6}Sb_2Te_5$ by adding vdW corrections (D3)[75] which have an effect very similar to that discussed above for GST523. Phase separation occurs on the same time scale of about 3 ns of the simulation without vdW corrections, while the onset of crystallization of GeTe increases from 2 ns (no vdW) to 27 ns.

The simulations of all three compositions show that at 600 K and on a time scale of a few ns, which are comparable to the operation conditions of the set process in the memory, the GGST alloy decomposes into amorphous GeSb and slightly Sb-doped GeTe regions. For the more rich $Ge_{9.6}Sb_2Te_5$ alloys, also regions of pure amorphous Ge are observed. After completion of the phase separation, crystal nucleation takes place in the GeTe-like regions and the crystal growth of cubic GeTe proceeds percolating through the whole cell, while the GeSb regions remain amorphous. These phases are intermediate products that differ from the thermodynamically stable phases that should form according to the convex hull construction, namely pure Ge and GST225 or Sb_2Te_3. Only on a longer time scale, not accessible by the MLIP-MD simulations, we expect to see a Ge/Sb exchange between the GeSb and GeTe regions to finally yield the thermodynamically stable products. The intermediate phases we see should correspond to the product of the set process in the memory. Indeed GeTe-like crystallites, possibly Sb-doped, were identified in EDX/EELS measurements in GGST memory cells in ref. 34. We note that diffraction data cannot easily discriminate between Sb-doped GeTe and stoichiometric GST alloys on the GeTe–Sb_2Te_3 tie-line due to the similarity of their lattice constants. On the other hand, as already mentioned, EELS and EDX measurements can only provide a composition averaged over different grains along the direction of the beam which introduces uncertainties in the measured composition of the crystallites. The present simulations thus provide an important support to the interpretation of the experimental characterization of the operation of the memory cell. We also remark that the formation of GeTe-like crystal in the decomposition of GGST was also predicted by thermochemical data based on DFT calculations in ref. 32. It was shown, that besides the thermodynamically stable compounds on the GeTe–Sb_2Te_3 tie-line, Sb-doped GeTe crystals in a large region of the phase diagram close to pure GeTe are highly favored in the decomposition of GST523[24] and GST725[23] because they lie close to the convex hull.[32] The formation of cubic GeTe-like crystals was also observed in the crystallization of thin films with composition along the Ge-GST225 tie-line,[20,31] and of two alloys with composition close to GST523 (at 300 °C) and GST725 (at 330 °C).[23] In another experimental work, the decomposition of GST523 at 450 °C was shown to yield GST213 and GST324 alloys,[24] which can again be seen as intermediate metastable phases toward the formation of the thermodynamically stable Ge and Sb_2Te_3. In contrast, we do not see the *Pnma* phase of GeTe found in ref. 31 in the crystallization of a Ge-rich alloy on the Ge-GST225 tie-line, but at a lower temperature and on a time scale of hours, which are far from the operation conditions of the memory that we addressed in our simulations. We note that the *Pnma* phase (often called γ-phase) is stabilized by pressure above 15 GPa in bulk GeTe at 300 K.[95] In all our simulations at constant volume that mimic the operation of the device, the pressure after decomposition of GGST and crystallization of GeTe is below 0.4 GPa. The density of the GeTe-like regions is 0.0339 atom per $Å^3$ which is lower than the experimental density of cubic (β) GeTe at the $\alpha \rightarrow \beta$ transition (0.0373 atom per $Å^3$).[93] The *Pnma* phase is also observed experimentally in the crystallization of slightly Te-rich $GeTe_x$ alloy,[96] while in our GeTe-like region the Ge/Te ratio is ≥ 1. Moreover, we note that the nature of the initial stages of phase separation and crystallization can depend on temperature. In our previous work on Ge_2Te we showed that at 600 K, segregation of most of the Ge in excess was observed to precede crystallization of nearly stoichiometric GeTe regions, while at 500 K nucleation of crystalline GeTe was observed to occur before phase separation, followed by a slow crystal growth due to the concurrent expulsion of Ge in excess. We found a similar behavior in GST725 at 500 K, in which the nucleation of GeTe-like crystals preceded phase separation, and then a much slower crystal growth was observed with the expulsion of Ge in excess. It is therefore conceivable that on a much longer time scale and at other temperatures, different intermediate products could form for some compositions, as observed experimentally. We remark once more that here we are interested in uncovering the kinetics of crystallization and phase separation on ns time scale of interest for the memory and not on the macroscopic time scale addressed in experiments on thin films. Note also that in our simulations we do not have free surfaces or interfaces with surrounding materials that could favor heterogeneous crystal nucleation.

5. Conclusions

In summary, we developed a MLIP for GGST alloys of interest for applications in phase change memories embedded in microcontrollers. The MLIP was generated with the DeePMD code by fitting a large database of DFT energies and forces of elemental, binary, stoichiometric ternary compounds in the Ge–Sb–Te ternary phase diagram and the GST523 non-stoichiometric Ge-rich alloy. The MLIP is highly transferable in large regions of the phase diagram around the compositions included in the dataset. In particular, we demonstrated the transferability to compositions on the Ge-GST225 and Ge–Sb_2Te_3 tie-lines. The MLIP was then exploited to simulate the crystallization with phase separation of the three compositions GST523, GST725 and $Ge_{9.6}Sb_2Te_5$, at 600 K and on the ns time scale which are comparable to the operation conditions of the memories. For all compositions, phase separation was completed in 1–3 ns yielding slightly Sb-doped GeTe and GeSb amorphous regions. In the more Ge-rich $Ge_{9.6}Sb_2Te_5$ alloys pure amorphous Ge regions were also observed. Then, crystal nucleation and growth take place in the GeTe-like region giving rise to a crystal percolating through the cell. The final products consisting of cubic Sb-doped GeTe and amorphous GeSb/Ge are intermediate metastable phases that form due to kinetic

effects, the thermodynamically stable phases being pure Ge and GST225 or Sb_2Te_3 that could form only in a much longer time scale. The cubic GeTe-like crystal is expected to form in the short time interval and at the operation temperature of the set process of the memory, as suggested by recent EELS/EDX measurements on the device.[34] Considering the uncertainties in the assignment of compositions by EELS/EDX in the presence of several grains, our results provide an important confirmation of the interpretation of the experimental data on the devices. Other intermediate products such as Sb-rich regions and Sb crystals that have been identified in the memories by EELS/EDX measurements in ref. 34, could result from the presence of a strong electric field and an inhomogeneous temperature field that might affect the decomposition process. MLIP can also be exploited to simulate the set process under these more realistic conditions of memory operation in very large models, as we recently did for stoichiometric GST225.[44] In fact, device-scale MD simulations can also include the effect of the electric field and of the temperature of the hot spot (heater) to provide information on how the programming protocol could affect the microstructure and then the drift in the set and reset states.

Author contributions

O. Abou El Kheir and M. Bernasconi contributed equally to the work. D. Baratella contributed to the development of the database and of the machine learning potential and partially to the simulations.

Conflicts of interest

There are no conflicts of interest to declare.

Data availability

The MLIP, the training DFT database, atomic trajectories of the phase separation and crystallization process, and a video of the relevant processes are available in the Materials Cloud repository at https://doi.org/10.24435/materialscloud:3j-n2.

Supplementary information (SI) is available. See DOI: https://doi.org/10.1039/d6tc01214k.

Code availability: LAMMPS, and DeePMD are free and open source codes available at https://lammps.sandia.gov and https://www.deepmd.org, respectively.

Acknowledgements

The project has received funding from European Union Next-Generation-EU through the Italian Ministry of University and Research under PNRR M4C2I1.4 ICSC Centro Nazionale di Ricerca in High Performance Computing, Big Data and Quantum Computing (Grant No. CN00000013). We acknowledge the CINECA award under the ISCRA initiative, for the availability of high-performance computing resources and support.

References

1 P. Fantini, *J. Phys. D: Appl. Phys.*, 2020, **53**, 283002.
2 M. Boniardi and M. Redaelli, *Phys. Status Solidi RRL*, 2025, **19**, 2500052.
3 A. Sebastian, M. Le Gallo, R. Khaddam-Aljameh and E. Eleftheriou, *Nat. Nanotechnol.*, 2020, **15**, 529.
4 G. S. Syed, M. Le Gallo and A. Sebastian, *Chem. Rev.*, 2025, **125**, 5163–5194.
5 P. Cappelletti, R. Annunziata, F. Arnaud, F. Disegni, A. Maurelli and P. Zuliani, *J. Phys. D*, 2020, **53**, 193002.
6 A. Redaelli, E. Petroni and R. Annunziata, *Mater. Sci. Semicond. Process.*, 2022, **137**, 106184.
7 M. Wuttig and N. Yamada, *Nat. Mater.*, 2007, **6**, 824.
8 P. Noé, C. Vallée, F. Hippert, F. Fillot and J.-Y. Raty, *Semicond. Sci. Technol.*, 2017, **33**, 013002.
9 W. Zhang, R. Mazzarello, M. Wuttig and E. Ma, *Nat. Rev. Mater.*, 2019, **4**, 150.
10 P. Zuliani, E. Varesi, E. Palumbo, M. Borghi, I. Tortorelli, D. Erbetta, G. D. Libera, N. Pessina, A. Gandolfo, C. Prelini, L. Ravazzi and R. Annunziata, *IEEE Trans. Electron Devices*, 2013, **60**, 4020.
11 P. Zuliani, E. Palumbo, M. Borghi, G. Dalla Libera and R. Annunziata, *Solid State Electron.*, 2015, **111**, 27.
12 E. Palumbo, P. Zuliani, M. Borghi and R. Annunziata, *Solid State Electron.*, 2017, **133**, 38.
13 G. Navarro, M. Coué, A. Kiouseloglou, P. Noé, F. Fillot, V. Delaye, A. Persico, A. Roule, M. Bernard, C. Sabbione, *et al.*, 2013 IEEE International Electron Devices Meeting, 2013, p. 21.
14 P. Noé, C. Sabbione, N. Bernier, N. Castellani, F. Fillot and F. Hippert, *Acta Mater.*, 2016, **110**, 142–148.
15 F. Arnaud, P. Zuliani, J. Reynard, A. Gandolfo, F. Disegni, P. Mattavelli, E. Gomiero, G. Samanni, C. Jahan, R. Berthelon, O. Weber, E. Richard, V. Barral, A. Villaret, S. Kohler, J. Grenier, R. Ranica, C. Gallon, A. Souhaite, D. Ristoiu, L. Favennec, V. Caubet, S. Delmedico, N. Cherault, R. Beneyton, S. Chouteau, P. Sassoulas, A. Vernhet, Y. Le Friec, F. Domengie, L. Scotti, D. Pacelli, J. Ogier, F. Boucard, S. Lagrasta, D. Benoit, L. Clement, P. Boivin, P. Ferreira, R. Annunziata and P. Cappelletti, 2018 IEEE International Electron Devices Meeting (IEDM), 2018, pp. 18.4.1-18.4.4.
16 F. Arnaud, P. Ferreira, F. Piazza, A. Gandolfo, P. Zuliani, P. Mattavelli, E. Gomiero, G. Samanni, J. Jasse, C. Jahan, J. P. Reynard, R. Berthelon, O. Weber, A. Villaret, B. Dumont, J. C. Grenier, R. Ranica, C. Gallon, C. Boccaccio, A. Souhaite, L. Desvoivres, D. Ristoiu, L. Favennec, V. Caubet, S. Delmedico, N. Cherault, R. Beneyton, S. Chouteau, P. O. Sassoulas, L. Clement, P. Boivin, D. Turgis, F. Disegni, J. L. Ogier, X. Federspiel, O. Kermarrec, M. Molgg, A. Viscuso, R. Annunziata, A. Maurelli, P. Cappelletti and E. Ciantar, 2020 IEEE International Electron Devices Meeting (IEDM), 2020, pp. 24.2.1-24.2.4.
17 M. Agati, M. Vallet, S. Joulié, D. Benoit and A. Claverie, *J. Mater. Chem. C*, 2019, **7**, 8720.

18 M. A. Luong, M. Agati, N. Ratel Ramond, J. Grisolia, Y. Le Friec, D. Benoit and A. Claverie, *Phys. Status Solidi RRL*, 2021, **15**, 2000471.

19 S. Privitera, V. Sousa, C. Bongiorno, G. Navarro, C. Sabbione, E. Carria and E. Rimini, *J. Phys. D*, 2018, **51**, 145103.

20 S. Privitera, I. López Garca, C. Bongiorno, V. Sousa, M. Cyrille, G. Navarro, C. Sabbione, E. Carria and E. Rimini, *J. Appl. Phys.*, 2020, **128**, 155105.

21 L. Prazakova, E. Nolot, E. Martinez, D. Rouchon, F. Fillot, N. Bernier, R. Elizalde, M. Bernard and G. Navarro, *Materialia*, 2022, **21**, 101345.

22 A. Díaz Fattorini, C. Chèze, I. Lopez García, C. Petrucci, M. Bertelli, F. Righi Riva, S. Prili, S. M. S. Privitera, M. Buscema, S. Sciuto, A. Amd Di Franco, G. D'Arrigo, M. Longo, S. De Simone, V. Mussi, E. Placidi, M.-C. Cyrille, N.-P. Tran, R. Calarco and F. Arciprete, *Nanomaterials*, 2022, **12**, 1340.

23 S. Cecchi, I. Lopez Garcia, A. M. Mio, E. Zallo, O. Abou El Kheir, R. Calarco, M. Bernasconi, G. Nicotra and S. M. Privitera, *Nanomaterials*, 2022, **12**, 631.

24 D. T. Yimam, A. J. T. Van Der Ree, O. Abou El Kheir, J. Momand, M. Ahmadi, G. Palasantzas, M. Bernasconi and B. J. Kooi, *Nanomaterials*, 2022, **12**, 1717.

25 H. Y. Cheng, J. Y. Wu, R. Cheek, S. Raoux, M. BrightSky, D. Garbin, S. Kim, T. H. Hsu, Y. Zhu, E. K. Lai, E. Joseph, A. Schrott, S. C. Lai, A. Ray, H. L. Lung and C. Lam, 2012 International Electron Devices Meeting, 2012, pp. 31.1.1-31.1.4.

26 G. Navarro, V. Sousa, P. Noe, N. Castellani, M. Coue, J. Kluge, A. Kiouseloglou, C. Sabbione, A. Persico, A. Roule, O. Cueto, S. Blonkowski, F. Fillot, N. Bernier, R. Annunziata, M. Borghi, E. Palumbo, P. Zuliani and L. Perniola, 2016 IEEE 8th International Memory Workshop (IMW), 2016, pp. 1-4.

27 L. Prazakova, E. Nolot, E. Martinez, F. Fillot, D. Rouchon, N. Rochat, M. Bernard, C. Sabbione, D. Morel, N. Bernier, A. Grenier, A.-M. Papon, M.-C. Cyrille and G. Navarro, *J. Appl. Phys.*, 2020, **128**, 215102.

28 J. Remondina, E. Rahier, M.-A. Luong, N. Ratel-Ramond, S. Ran, D. Grosso, C. Mocuta, A. Portavoce, Y. Le Friec, D. Benoit, E. Petroni, A. Claverie and M. Putero, *Phys. Status Solidi RRL*, 2025, **19**, 2500035.

29 O. Thomas, C. Mocuta, M. Putero, M.-I. Richard, P. Boivin and F. Arnaud, *Microelectron. Eng.*, 2021, **244–246**, 111573.

30 T. H. Lee, D. Loke and S. R. Elliott, *Adv. Mater.*, 2015, **27**, 5477–5483.

31 E. Rahier, M.-A. Luong, S. Ran, N. Ratel-Ramond, S. Saha, C. Mocuta, D. Benoit, Y. Le-Friec and A. Claverie, *Phys. Status Solidi RRL*, 2023, **17**, 2200450.

32 O. Abou El Kheir and M. Bernasconi, *Nanomaterials*, 2021, **11**, 2382.

33 O. Abou El Kheir, D. Dragoni and M. Bernasconi, *Phys. Rev. Mater.*, 2021, **5**, 95004.

34 S. Ran, E. Petroni, L. Laurin, M. Baldo, A. Serafini, M.-A. Luong, A. Motta, A. Redaelli and A. Claverie, *Sci. Rep.*, 2025, **15**, 11357.

35 L. Laurin, M. Baldo, E. Petroni, G. Samanni, L. Turconi, A. Motta, M. Borghi, A. Serafini, D. Codegoni, M. Scuderi, S. Ran, A. Claverie, D. Ielmini, R. Annunziata and A. Redaelli, 2023 IEEE International Reliability Physics Symposium (IRPS), 2023, pp. 1-7.

36 L. Sun, Y.-X. Zhou, X.-D. Wang, Y.-H. Chen, V. L. Deringer, R. Mazzarello and W. Zhang, *npj Comput. Mater.*, 2021, **7**, 1.

37 J. Behler and M. Parrinello, *Phys. Rev. Lett.*, 2007, **98**, 146401.

38 A. P. Bartók, M. C. Payne, R. Kondor and G. Csányi, *Phys. Rev. Lett.*, 2010, **104**, 136403.

39 R. Jacobs, *et al.*, *Curr. Opin. Solid State Mater. Sci.*, 2025, **35**, 101214.

40 B. Kalita, H. Gokcan and O. Isayev, *Nat. Comp. Sci.*, 2025, **5**, 1120–1132.

41 G. C. Sosso, G. Miceli, S. Caravati, F. Giberti, J. Behler and M. Bernasconi, *J. Phys. Chem. Lett.*, 2013, **4**, 4241–4246.

42 G. C. Sosso, M. Salvalaglio, J. Behler, M. Bernasconi and M. Parrinello, *J. Phys. Chem. C*, 2015, **119**, 6428–6434.

43 O. Abou El Kheir, L. Bonati, M. Parrinello and M. Bernasconi, *npj Comput. Mater.*, 2024, **10**, 33.

44 O. Abou El Kheir and M. Bernasconi, *Adv. Electr. Mater.*, 2025, **11**, e2500110.

45 Y. Zhou, D. F. T. du Toit, S. R. Elliott, W. Zhang and V. L. Deringer, *Nat. Commun.*, 2025, **16**, 8688.

46 J. Su, Z. Zhang, X. Wan, W. Yu, A. Wang, H. Zhong, J. Robertson and Y. Guo, *Appl. Phys. Lett.*, 2023, **122**, 252102.

47 D. Baratella, O. Abou El Kheir and M. Bernasconi, *Acta Mater.*, 2025, **284**, 120608.

48 L. Zhang, J. Han, H. Wang, R. Car and W. E, *Phys. Rev. Lett.*, 2018, **120**, 143001.

49 J. Zeng, D. Zhang, D. Lu and P. Mo, *et al.*, *J. Chem. Phys.*, 2023, **159**, 054801.

50 L. Henry, N. Bernier, M. Jacob, G. Navarro, L. Clément, J.-L. Rouviére and E. Robin, *Acta Mater.*, 2020, **201**, 72–78.

51 H. Wang, L. Zhang, J. Han and W. E, *Comput. Phys. Commun.*, 2018, **228**, 178.

52 J. VandeVondele, M. Krack, F. Mohamed, M. Parrinello, T. Chassaing and J. Hutter, *Comput. Phys. Commun.*, 2005, **167**, 103–128.

53 J. P. Perdew, K. Burke and M. Ernzerhof, *Phys. Rev. Lett.*, 1996, **77**, 3865.

54 S. Goedecker, M. Teter and J. Hutter, *Phys. Rev. B: Condens. Matter Mater. Phys.*, 1996, **54**, 1703.

55 M. Krack, *Theor. Chem. Acc.*, 2005, **114**, 145.

56 A. Laio and M. Parrinello, *Proc. Natl. Acad. Sci. U. S. A.*, 2002, **99**, 12562–12566.

57 L. Bonati and M. Parrinello, *Phys. Rev. Lett.*, 2018, **121**, 265701.

58 H. Niu, L. Bonati, P. M. Piaggi and M. Parrinello, *Nat. Commun.*, 2020, **11**, 2654.

59 A. P. Thompson, H. M. Aktulga, R. Berger, D. S. Bolintineanu, W. M. Brown, P. S. Crozier, P. J. in't Veld, A. Kohlmeyer, S. G. Moore, T. D. Nguyen, R. Shan, M. J. Stevens, J. Tranchida, C. Trott and S. J. Plimpton, *Comp. Phys. Comm.*, 2022, **271**, 108171.

60 P. J. Steinhardt, D. R. Nelson and M. Ronchetti, *Phys. Rev. B: Condens. Matter Mater. Phys.*, 1983, **28**, 784–805.

61 P. R. ten Wolde, M. J. Ruiz-Montero and D. Frenkel, *J. Chem. Phys.*, 1996, **104**, 9932.
62 A. I. Bartók, R. Kondor and G. Csányi, *Phys. Rev. B:Condens. Matter Mater. Phys.*, 2013, **87**(18), 1–16.
63 I. Jolliffe, *Principal component analysis*, Springer Verlag, Berlin, 2nd edn, 2002.
64 A. K. Jain, M. N. Murty and P. J. Flynn, *ACM Comput. Surv.*, 1999, **31**, 264–323.
65 J. Laakso, L. Himanen, H. Homm, E. V. Morooka, M. O. Jäger, M. Todorovic and P. Rinke, *J. Chem. Phys.*, 2023, **158**, 234802.
66 L. Himanen, M. O. J. Jäger, E. V. Morooka, F. Federici Canova, Y. S. Ranawat, D. Z. Gao, P. Rinke and A. S. Foster, *Comp. Phys. Comm.*, 2020, **247**, 106949.
67 A. H. Larsen, *et al.*, *J. Phys.: Condens. Matter*, 2017, **29**, 273002.
68 F. Pedregosa, G. Varoquaux, A. Gramfort, V. Michel, B. Thirion, O. Grisel, M. Blondel, P. Prettenhofer, R. Weiss, V. Dubourg, J. Vanderplas, A. Passos, D. Cournapeau, M. Brucher, M. Perrot and E. Duchesnay, *J. Mach. Learn. Res.*, 2011, **12**, 2825–2830.
69 S. Urata, *J. Phys. Chem. C*, 2022, **126**, 21507–21517.
70 B. Zhai and H. Wang, *Comput. Mater. Sci.*, 2023, **216**, 111843.
71 J. Liu, R. Liu, Y. Cao and M. Chen, *Phys. Chem. Chem. Phys.*, 2023, **25**, 983–993.
72 X. Huang, K. Luo, Y. Shen, Y. Yue and Q. An, *Energy AI*, 2023, **11**, 100210.
73 J. R. Errington and P. G. Debenedetti, *Nature*, 2001, **409**, 318.
74 S. Caravati, M. Bernasconi, T. Kühne, M. Krack and M. Parrinello, *Appl. Phys. Lett.*, 2007, **91**, 171906.
75 S. Grimme, J. Antony, S. Ehrlich and H. Krieg, *J. Chem. Phys.*, 2010, **132**, 154104.
76 M. Rizzi, N. Ciocchini, S. Caravati, M. Bernasconi, P. Fantini and D. Ielmini, 2014 IEEE International Electron Devices Meeting, 2014, p. 29.6.1.
77 G. C. Sosso, G. Miceli, S. Caravati, J. Behler and M. Bernasconi, *Phys. Rev. B: Condens. Matter Mater. Phys.*, 2012, **85**, 174103.
78 D. Dragoni, J. Behler and M. Bernasconi, *Nanoscale*, 2021, **13**, 16146–16155.
79 G. C. Sosso, J. Behler and M. Bernasconi, *Phys. Status Solidi B*, 2012, **249**, 1880.
80 T. Bryk, I. Ilenkov and A. Seitsonen, *J. Phys.: Condens. Matter*, 2023, **35**, 154003.
81 H. Weber, M. Schumacher, P. Jóvári, Y. Tsuchiya, W. Skrotzki, R. Mazzarello and I. Kaban, *Phys. Rev. B*, 2017, **96**, 054204.
82 J. Akola and R. Jones, *Phys. Rev. B: Condens. Matter Mater. Phys.*, 2007, **76**, 235201.
83 J. Hegedüs and S. Elliott, *Nat. Mater.*, 2008, **7**, 399.
84 D. Acharya, O. Abou El Kheir, S. Marcorini and M. Bernasconi, *Nanoscale*, 2025, **17**, 13828–13841.
85 S. Grimme, *J. Comput. Chem.*, 2006, **27**, 1787–1799.
86 S. Marcorini, R. Pomodoro, O. Abou El Kheir and M. Bernasconi, *J. Chem. Phys.*, 2025, **163**, 154501.
87 G. E. Ghezzi, J. Y. Raty, S. Maitrejean, A. Roule, E. Elkaim and F. Hippert, *Appl. Phys. Lett.*, 2011, **99**, 151906.
88 K. Laaziri, S. Roorda and J. Baribeau, *J. Non-Cryst. Solids*, 1995, **191**, 193–199.
89 K. J. Singh, R. Satoh and Y. Tsuchiya, *J. Phys. Soc. Jpn.*, 2003, **72**, 2546–2550.
90 A. Stukowski, *Modelling Simul. Mater. Sci. Eng.*, 2010, **18**, 015012.
91 S. Perego, D. Dragoni, S. Gabardi, D. Campi and M. Bernasconi, *Phys. Stat. Solidi RRL*, 2023, **13**, 2200433.
92 T. Chattopadhyay, J. X. Boucherle and H. G. von Schnering, *J. Phys. C-Solid State Phys.*, 1987, **20**, 1431.
93 T. Chatterji, C. M. N. Kumar and U. D. Wdowik, *Phys. Rev. B: Condens. Matter Mater. Phys.*, 2015, **91**, 054110.
94 J. Goldak, C. S. Barrett, D. Innes and W. Youdelis, *J. Chem. Phys.*, 1966, **44**, 3323–3325.
95 A. Pawbake, C. Bellin, L. Paulatto, K. Béneut, J. Biscaras, C. Narayana, D. J. Late and A. Shukla, *Phys. Rev. Lett.*, 2019, **122**, 145701.
96 A. Schlieper, Y. Feutelais, S. Fries, B. Legendre and R. Blachnik, *Calphad*, 1999, **23**, 1–18.

